Liquid Viscosity Measurement Using a Vibrating Flexure Hinged Structure and a Fiber-Optic Sensor

Jinyu Ma, Xinjing Huang, Hyungdae Bae, Yelong Zheng, Cong Liu, Meirong Zhao, and Miao Yu

***Abstract*— A novel viscosity measurement system based on a miniature 3D printed parallelogram flexure hinge structure and a fiber-optic sensor is developed. Lorentz forces are applied to excite the structure vibration at various frequencies, and the fiber-optic sensor is used to measure the amplitude and phase responses without the electromagnetic interference. The system is modeled as a single oscillator by taking into account the liquid-induced mass and damping as well as the additive stiffness due to the liquid viscoelasticity. By curve fitting of the experimentally obtained amplitude and phase responses based on the analytical model, the viscosity and the additive stiffness can be obtained. This method can help differentiate the effect of the viscosity and elasticity on the response of the sensing structure. By implementing this method, accurate viscosity measurements over a large range of 1–1045 mPa·s are demonstrated with the errors of <3.7% for all the test samples. It is also confirmed in the experiment that the liquid-induced additive stiffness is strongly related to the liquid storage modulus.**

***Index Terms*— Viscosity, elasticity, flexure hinge, optic fiber, vibrating slice, electromagnetic actuation.**

I. Introduction

THERE has been increasing demand for precise and fast measurements of liquid properties, such as density, compressibility, and viscosity, in process industry, analytical chemistry, biochemistry, and bio-analytics [1]. Specifically, for viscosity measurements, standard laboratory viscosity instruments mainly utilize conventional methods [2], such as capillary viscometers, falling sphere viscometers, falling sinker viscometers, rotary viscometers, and vibrational viscometers. Among these conventional viscometers, vibrational viscometers have the advantages of compactness, being less susceptible to pressure gradients, low time consuming, and low heat generation and leakage [3]. For vibrational viscosity measurement devices, a resonant mechanical structure is often utilized to interact with a liquid, and the viscosity and density of the liquid can be determined by examining the shift of the resonance frequency f_r [4] and the change of the quality factor (Q-factor) [5], [6], both of which can be obtained from frequency response curves of the structure. However, this method suffers from low accuracy for liquids with extremely high viscosities, and thus it can only be used to measure viscosity within a certain range. Furthermore, for viscoelastic fluids, the fluid elasticity is another factor that can affect the resonance frequency. It is therefore no longer applicable to obtain the viscosity by measuring the resonance frequency.

On the other hand, miniaturized viscosity measurement devices are desirable as they require small sample volumes [7]. Several types of miniaturized vibrational viscosity sensors have been reported, including vibrating cantilevers [8], plates [9], wires [10], and membranes [5], [11]. These sensors require only several milliliters of sample. However, they suffer from the repeatability and stability issues of resonance frequency measurements caused by cross sensitivities to other parameters such as thermal stresses [5], [11]. Miniaturized viscosity sensors based on ultrasonic principles, including thickness shear mode (TSM) quartz resonators [12] and surface acoustic wave (SAW) devices [13], have also been demonstrated. However, due to the high frequency (several MHz) and small penetration depth (a few microns), these devices are susceptible to surface contamination and are not suitable for complex liquids, such as emulsions whose viscosity is too large or suspensions in which the particle size is close to or greater than the penetration depth of the acoustic shear wave [14].

It is worth noting that most viscosity sensing structures are actuated by electrical or electromagnetic excitations, such as the interdigital transducer in surface acoustic wave (SAW) devices [15] and electromagnetic coils in resonant steel tuning forks [16]. In this case, different displacement sensing devices (e.g., hall sensor [17], capacitive sensor [18], and eddy current sensor [19]) are used.

In this paper, we present a novel parallelogram flexure hinge structure (PFHS) to realize a miniature system for viscosity measurement. The PFHS is a 3D printed structure, which does not require any assembly and lubrication [20]. Furthermore, the PFHS is combined with a fiber optic sensor,

Manuscript received February 10, 2016; revised April 10, 2016; accepted May 2, 2016. Date of publication May 4, 2016; date of current version June 2, 2016. This work was supported by the National Key Scientific Instrument and Equipment Development Project under Grant 2013YQ030915. The associate editor coordinating the review of this paper and approving it for publication was Prof. Bernhard Jakoby. *(Corresponding author: Miao Yu.)*

J. Ma is with the State Key Laboratory of Precision Measurement Technology and Instrument, Tianjin University, Tianjin 300072, China, and also with the Department of Mechanical Engineering, University of Maryland, College Park, MD 20742 USA (e-mail: jyma2014@163.com).

X. Huang, Y. Zheng, C. Liu, and M. Zhao are with the State Key Laboratory of Precision Measurement Technology and Instrument, Tianjin University, Tianjin 300072, China (e-mail: huangxinjing007@gmail.com; zhengyelongby@163.com; liucong0525@163.com; meirongzhao@tju.edu.cn).

H. Bae and M. Yu are with the Department of Mechanical Engineering, University of Maryland, College Park, MD 20742 USA (e-mail: abebae0691@gmail.com; mmyu@umd.edu).

This paper has supplementary downloadable multimedia material available at http://ieeexplore.ieee.org provided by the authors. The Supplementary Material contains the derivation of (10) and the method of curve fitting. This material is 277 KB in size.

Digital Object Identifier 10.1109/JSEN.2016.2562740

1558-1748 © 2016 IEEE. Personal use is permitted, but republication/redistribution requires IEEE permission.
See http://www.ieee.org/publications_standards/publications/rights/index.html for more information.

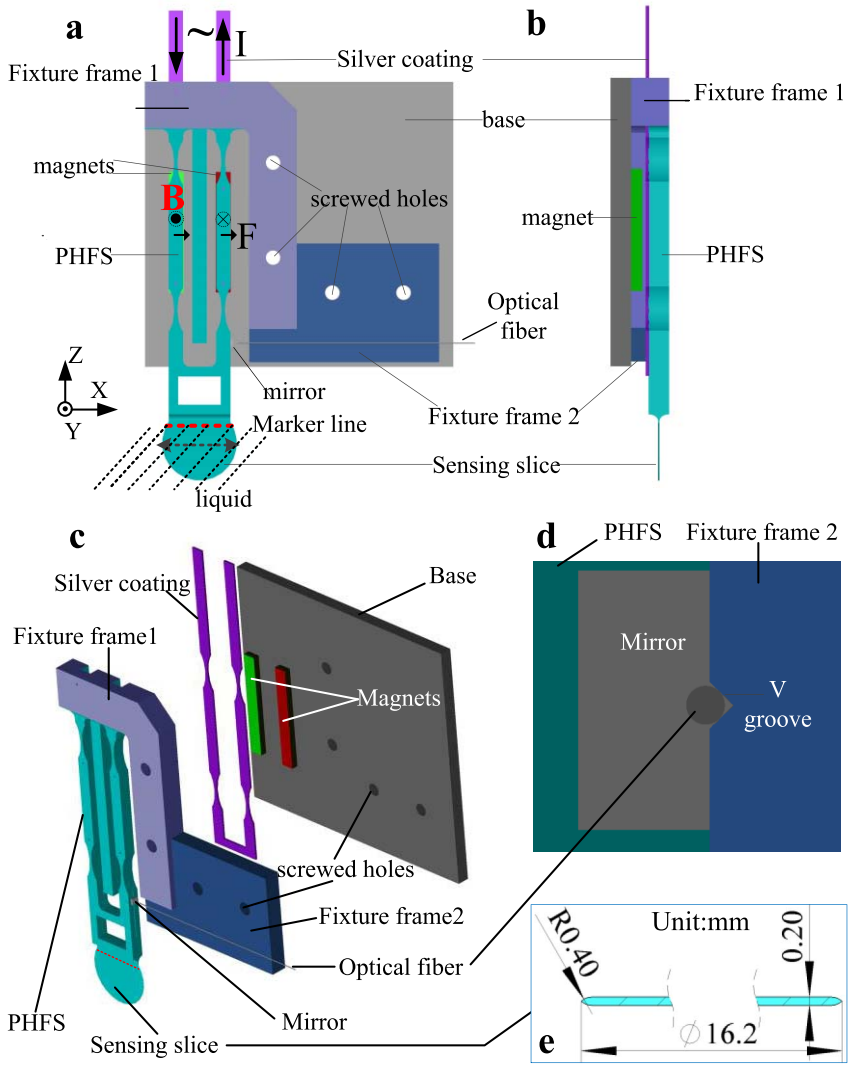

Fig. 1. Schematic of the entire sensing device. (a) Front view. I, B and F represent the sinusoidal current, the magnetic flux density, and the Lorentz-force, respectively. (b) Side view. (c) Assembly diagram. (d) Blow-up of right side view to show the mirror and the fiber in the groove. (e) Cross-sectional view of the slice. The sensing slice with a tapered edge has a diameter of 16.2 mm and a center thickness of 0.2 mm. The dimensions of the magnets are 25 mm × 3 mm × 2 mm.

which can achieve high precision non-contact measurement of the structure deflection without electromagnetic interference. In terms of data processing, rigorous mathematical formulae are derived based on a single oscillator model of the system, which can be used to directly solve the viscosity and the additive stiffness due to the elasticity of the fluid (Newtonian or non-Newtonian fluid), resulting in a wide measurement range and high accuracy.

II. Device Design and Fabrication

A. Configuration of Viscosity Measurement Device

The schematic of the entire viscosity measurement device is depicted in Fig. 1. As shown in Fig. 1 a, the device is composed of Fixture frame 1, Fixture frame 2, PFHS, a sensing slice, and a fiber optic sensor. The device is 3D printed into a monolithic structure that is fixed on an aluminum base using screws. The different colors in Fig. 1 are used to distinguish the different functional parts. The PFHS as well as the sensing slice can oscillate in the X direction under a Lorentz driving force. The oscillating displacement is measured by using the fiber optic sensor. Fig. 1 e shows the cross-sectional view of the sensing slice, which has a thickness of 0.2 mm in the middle and a tapered edge. The area of the sensing slice below the marker line is immersed in the testing liquid, and the interaction between the slice and the liquid will affect the oscillation of the PFHS. Therefore, by measuring the frequency response of the PFHS, the characteristics of the liquid can be obtained as detailed in Sections III and IV.

As shown in Fig. 1 b, Fixture frame 1 is designed to be thicker than the PFHS so that the PFHS can be suspended, avoiding any contact with the base or magnets. The assembly diagram is shown in Fig. 1 c. Underneath the PFHS, two magnets with different poles are glued onto the base, and the gap between the magnets and the PFHS is controlled to be ~0.5 mm in the Y direction to provide a large magnetic field (about 0.2 T). Silver coating is sprayed onto the inside surface (facing the magnets) of the PFHS to make a conductive path. An AC current runs through the silver coating. The

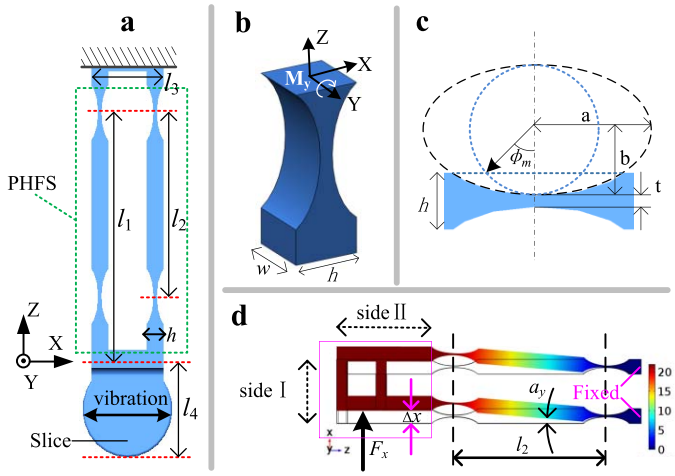

Fig. 2. Schematic of PFHS. (a) PFHS with a sensing slice. Arrows on the slice represent the oscillation direction. $l_1 = 53$ mm, $l_2 = 31$ mm, $l_3 = 13$ mm, $l_4 = 16.8$ mm, $h = 3$ mm. The green dashed line defines the PHFS. (b) 3D view of the EAFH. $w = 3$ mm. (c) Geometry of the EAFH. $a = 5$ mm, $b = 2$ mm, $t = 0.34$ mm. (d) Simulation results of PFHS displacement at its fundamental frequency (obtained by using COMSOL software). The simulated PHFS is fixed at the right end. The solid black outline represents the static equilibrium of PFHS, and the colors represent vibrational displacement.

magnetic field of the magnets interacts with the oscillating current, resulting in a dynamic Lorentz force F acting on the PFHS, and F is [10]

$$F = BIL, \tag{1}$$

where B is the magnitude of the Y-oriented magnetic field, I is the sinusoidal excitation current, and L is the effective length of the silver coating. Under this force, the PFHS is actuated and the sensing slice will oscillate in the X direction.

As shown in Fig. 1 c, the PFHS vibration amplitude is measured by a reflective intensity modulated (RIM) fiber optic sensor. A small mirror (1.5 mm × 1.5 mm × 0.5 mm) is glued onto the right side surface of the PFHS as the reflective surface. It is made of a silicon substrate with a 0.2 μm-thick aluminum film coated on its surface by vacuum ion plating. In order to precisely control the position of the optical fiber, a V groove with an open width of 275 μm is printed on Fixture frame 2, as shown in Fig. 1 d, which is perpendicular to the mirror surface and aligned with the mirror center. A single mode optical fiber is placed into the V groove and fixed with drops of UV glue. The fiber tip is 760 μm away from the mirror.

B. Design and Parametric Study of PFHS

As the most important component of the viscosity measurement device, the PFHS, as shown in Fig. 2, serves as a resonator, which will oscillate at its fundamental mode in the X direction. It is advantageous to use the PFHS as a resonator, which ensures high precision and high stability motion. In fact, flexure hinges have been used in many applications where high precision and sensitivity are required [21], such as fine positioning stages, mass balances, and X-ray interferometers. As shown in Fig. 2 a-c, the PFHS consists of four elliptical arc flexure hinges (EAFH). EAFHs are adopted due to its flexibility and long fatigue life compared with circular or corner-filleted flexure hinges [22].

Unlike vibrating cantilevers, there is no rotation at the end of the PFHS when the PFHS vibrates in the X direction. This can be seen from the simulation results shown in Fig. 2 d, in which the structure is excited by the Lorentz force F at its fundamental frequency. Benefiting from the parallelogram design, side I and side II (shown in Fig. 2 d) of the PFHS are always parallel to the X axis and the Z axis, respectively. A mirror is attached to side II, which can only have translational displacement in the X axis without any rotation. This feature will help facilitate accurate displacement measurement (without rotational errors) from a fiber optic sensor, which is used to track the mirror displacement, and thus perform non-contact measurement of the PFHS vibration amplitude.

The PFHS is designed to have a small bending stiffness along the X axis, but a large bending stiffness along the Y axis and a large torsional stiffness about the Z axis. This will ensure a large vibration amplitude in the X direction and suppress undesirable vibrations in the Y and Z directions.

Compliance is an important parameter in the design of PFHS, as it determines the natural frequency and sensitivity of the system to the fluid properties. Since the left part of PFHS has only translational displacement without rotation, as shown in Fig. 2 d, under an effective force F_x applied along the X axis, the translational displacement is Δx, and the rotation angle of each hinge about the Y axis is obtained as

$$\alpha_y \approx \sin \alpha_y = \frac{\Delta x}{l_2}, \tag{2}$$

where l_2 is the distance between two EAFHs (see Fig. 2 a and d). The total potential energy of the four deformed hinges is:

$$\frac{1}{2}\frac{1}{C_x}\Delta x^2 = 4\left(\frac{1}{2}\frac{1}{\theta_y}\alpha_y^2\right), \tag{3}$$

where C_x and θ_y are the translational compliance of the PFHS in the X direction and the angular compliance about the Y axis of EAFH, respectively. Substituting Eq.(2) into (3), it is obtained that

$$C_x = \frac{l_2^2}{4}\theta_y. \tag{4}$$

The angular compliance θ_y is obtained as [23]:

$$\theta_y = \frac{\alpha_y}{M_y} = \frac{12a}{Ewb^3}\int_{-\phi_m}^{\phi_m} \frac{\cos\phi}{g^3(\phi)} d\phi. \tag{5}$$

Here, M_y denotes the moment acting on an EAFH about the Y axis, and E is the Young's modulus. Parameters a, b, and w represent the semi-major axis, semi-minor axis of the side ellipse, and width of the EAFH, respectively. ϕ_m is defined in Fig. 2 c, and

$$\phi_m = \cos^{-1}\left(\frac{b - \frac{h-t}{2}}{b}\right) = \cos^{-1}\left(1 - \frac{h-t}{2b}\right), \tag{6}$$

$$g(\phi) = 2 + t/b - 2\cos\phi, \tag{7}$$

where h and t are the thickness and neck thickness of the EAFH, respectively.

It is noted that C_X is related to six geometric parameters l_2, w, a, b, h and t. Among these parameters, we first fixed

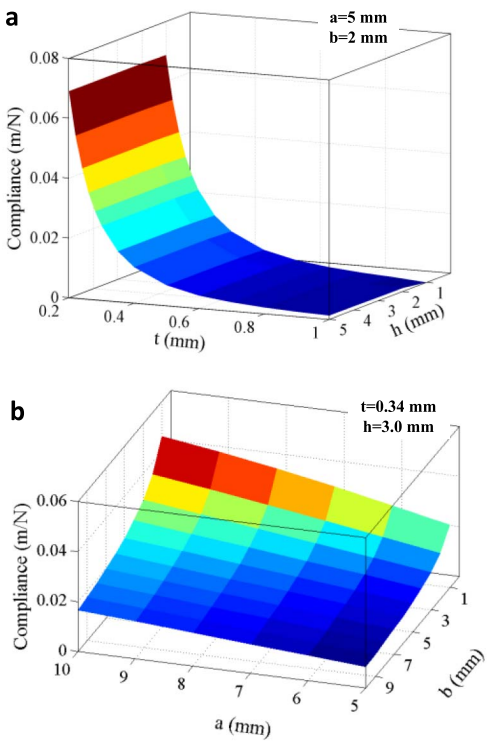

Fig. 3. The influence of a, b, t, h on the compliance. (a) C_X versus t and c for $a = 5$ mm and $b = 2$ mm. (b) C_X versus a and b for $t = 0.34$ mm and $h = 3.0$ mm.

two parameters, $l_2 = 31$ mm and $w = 3$ mm, which can generally determine the overall size of the PFHS. Then, a parametric study was carried out to examine the effects of other parameters a, b, t, and h on C_X.

As shown in Fig. 3 a, the compliance decreases rapidly with the increase of t, which is the most influential parameter among a, b, t, and h. In fact, the compliance is decreasing with the neck thickness in an approximately $1/t^3$ manner since the main contributor is the neck's second moment of area I_{neck} ($I_{\text{neck}} = wt^3/12$). Furthermore, the effect of h is negligibly small for the simulated range. Note that h affects the integral boundary ϕ_{m} in Eq. (5) and ϕ_{m} increases with the increase of h. For $h = 1$ mm, the smallest simulation value, the integral boundary $\varphi_{\text{m}} = 33°$. On the other hand, the integrand in Eq.(5) is centrally distributed in the range of $-30°$ to $30°$. Therefore, for $h \geqslant 1$ mm, the integral of Eq. (5) varies little with respect to h. In Fig. 3 b, the compliance is shown to decrease with the decrease of a and increase of b. Based on Fig. 3 a and b, we can design a set of suitable parameters for a preferable C_X.

As the influence of h on C_X is negligible, we first let $h = 3$ mm. The effective mass m_0 of the PFHS was calculated with $l_2 = 31$ mm, $w = 3$ mm and $h = 3$ mm, by using the following kinetic energy equation [24]

$$\begin{aligned}&\frac{1}{2}m_0\dot{u}(0)^2\\&= \int_{-l_4}^{l_1}\frac{1}{2}\rho_l(z)\dot{u}(z)^2dz\\&= \int_{-l_4}^{l_1-l_2}\frac{1}{2}\rho_l(z)\dot{u}(0)^2dz + \int_{l_1-l_2}^{l_1}\frac{1}{2}\rho_l(z)\left(\frac{l_1-z}{l_2}\dot{u}(0)\right)^2dz,\end{aligned} \tag{8}$$

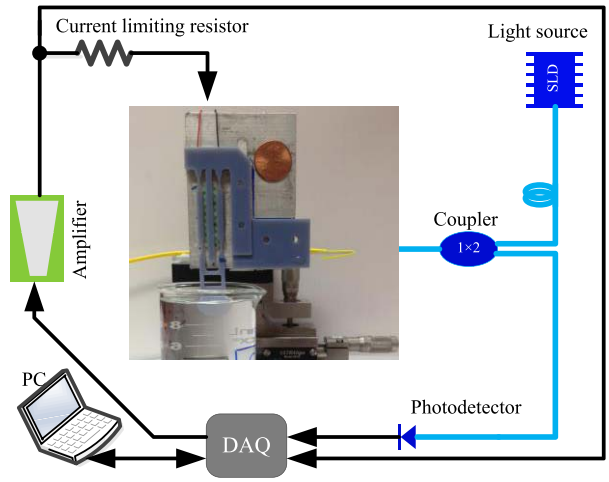

Fig. 4. Schematic of experimental arrangement.

where $u(0)$ and $u(z)$ are the displacements at the positions 0 and z, and ρ_l is the linear density of the 3D printing material. l_1, l_2, l_4 are denoted in Fig. 2 a. It was obtained that $m_0 = 0.7$ g. The natural frequency f of the PFHS was designed to be between 40 Hz~50 Hz. By using [24]

$$2\pi f = \sqrt{\frac{1}{C_X m_0}}, \tag{9}$$

the range of C_X was obtained to be 0.0144 m/N~0.0226 m/N. Based on the above analysis, the other design parameters were chosen to be $a = 5$ mm, $b = 2$ mm, and $t = 0.34$ mm. For the 3D printing material (RGD525) with $E = 3.2$ GPa, $\rho = 1.18$ g/cm^3, and $G = 1.1852$ GPa, the corresponding compliance was calculated as 0.0181 m/N based on Eq. (4). The simulation results show that the bending compliance in the X direction, 0.017912 m/N, is about four times as high as that in the Y direction, 0.004555 m/N. The torsional compliance about the Z axis is only 17.68154 rad/N•m. The compliance in the X direction obtained from simulations (0.017912 m/N) is very close to the value (0.0181 m/N) calculated by using Eq. (4).

C. Measurement System

The experimental arrangement for viscosity measurement is illustrated in Fig. 4. Frequency-swept harmonic excitation signals were generated by using a DAQ (USB6259) via a LABVIEW program on a PC. The signals were then applied to the silver coating via a current limiting resistor. The generated Lorentz-forces F were used to actuate the PFHS and the sensing slice, which can oscillate in the X direction. The oscillation amplitude was measured by using the reflective intensity modulated fiber optic sensor. The optical system consists of a broadband light source, a 1×2 coupler, and a photo-detector. The output signal from the photo-detector and the driving signal were simultaneously collected by the DAQ for further data processing.

The displacement measurement principle from the fiber optic sensor is illustrated in Fig. 5 a. For a constant input light intensity P_{in}, the distance l between the fiber endface and the

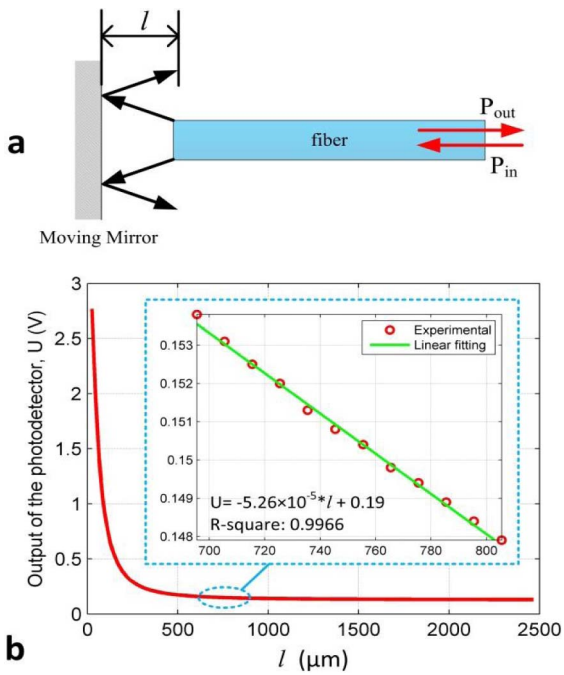

Fig. 5. (a) Schematic of reflective intensity modulated fiber optic sensor. (b) Experiment result of photo-detector output voltage versus the distance l.

mirror fixed on the PFHS can be obtained by characterizing the received reflection intensity P_{out} from the same fiber. The relationship between P_{out} and l is:

$$P_{out} = P_{in}\frac{r - re^{-2\left(1+\left(\frac{2l\lambda}{\pi a_0^2}\right)^2\right)^{-1}}}{1 - e^{-2}}, \tag{10}$$

where r is the mirror reflection coefficient, λ is the wavelength, and a_0 is the beam waist. The derivation of Eq. (10) is provided in the supplementary information.

The photo-detector converts P_{out} into an amplified voltage signal U. For an input power of 1 mW from the light source, the measured photo-detector output voltage as a function of the mirror displacement is shown in Fig. 5 b. For the measured displacement range of 100 μm to 2.5 mm, the plot is nonlinear. In order to obtain a good linearity and a relatively high sensitivity, we chose 760 μm as the initial gap displacement that was corresponding to the equilibrium position of the vibrational structure. As shown in the inset of Fig. 5 b, in the range of 700 μm to 800 μm, the output voltage of the photo-detector exhibits good linearity with the distance change.

III. Modeling

The sensor is modeled as a mass-spring-damper system, which oscillates along the X axis, as illustrated in Fig. 6. The fundamental mode of the sensor is utilized as the excitation mode. Due to the parallelogram structure, the beam (i.e., side I in Fig.2 d) remains parallel with the X axis when oscillating. Furthermore, the viscosity is assumed to be independent of frequency [25], [26]. This assumption was also used in previous studies [4], [5], [8], [10], [11], [16].

When the sensing slice is immersed in a liquid and driven by an effective harmonic force $F_H = H\cos(\omega t)$, the equation

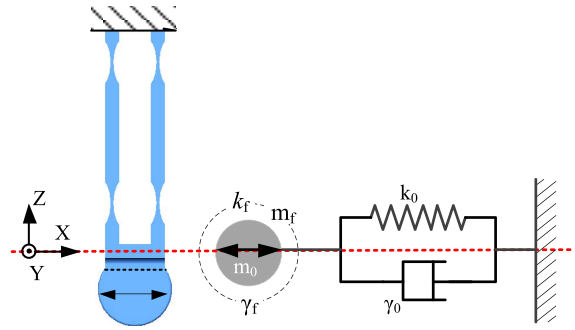

Fig. 6. Schematic of the mass-spring-damper oscillator model of the sensor.

of motion for the oscillator in the X direction can be written as

$$(m_0 + m_f)\frac{d^2u}{dt^2} + (\gamma_0 + \gamma_f)\frac{du}{dt} + (k_0 + k_f)u = H\cos(\omega t), \tag{11}$$

where H, ω, u are the effective excitation force amplitude, the excitation angular frequency, and the displacement of the slice, respectively, m_0, k_0, γ_0 are the effective mass, effective stiffness, and intrinsic damping coefficient of the PFHS, respectively, and m_f, γ_f, and k_f are the fluid induced mass, damping coefficients, and additive stiffness due to the liquid elasticity, respectively. The analytical expressions for m_f and γ_f are assumed to be the following [27], [28]:

$$m_f = S\sqrt{\frac{\eta_f \rho_f}{2}}\omega^{-1/2}, \tag{12}$$

$$\gamma_f = S\sqrt{\frac{\eta_f \rho_f}{2}}\omega^{1/2}, \tag{13}$$

where ρ_f, η_f, S are the density of the fluid, the dynamic viscosity of the fluid, and the solid-liquid interaction surface, respectively. As shown in Fig.1 e, the edge of the slice is tapered to help reduce the normal force acting on the solid-liquid interface so that a nearly perfect shearing wave propagation can be obtained.

The steady state solution of Eq. (11) is

$$u = A\cos(\omega t + \phi), \tag{14}$$

where

$$A = \frac{H/m_0}{[(\frac{k_0+k_f}{m_0} - (1+\frac{m_f}{m_0})\omega^2)^2 + (\frac{\gamma_0+\gamma_f}{m_0})^2\omega^2]^{1/2}}, \tag{15}$$

$$\phi = \arctan\frac{(\frac{\gamma_0+\gamma_f}{m_0})\omega}{\frac{k_0+k_f}{m_0} - (1+\frac{m_f}{m_0})\omega^2}. \tag{16}$$

Let

$$h = \frac{H}{m_0}, \tag{17}$$

$$K_{m_0} = \frac{k_0 + k_f}{m_0}, \tag{18}$$

$$\beta = \frac{\gamma_0}{m_0}, \tag{19}$$

TABLE I
VISCOSITY-DENSITY-STIFFNESS VALUES OF DIFFERENT SAMPLES AT 20 °C

NO.	Samples	η_a (mPa·s)	ρ_f (g/cm^3)	k_f/S[2] (N/m/m^2)	G' (Pa)	η_{m1}*	η_{m2}*	$\lvert\eta_a-\eta_{m1}\rvert/\eta_a$	$\lvert\eta_a-\eta_{m2}\rvert/\eta_a$
1#	air	0.018	0.0013	0	--	--	--	--	--
2#	water	1	0.998	0	--	0.998	0.99	0.2%	1%
3#	0.3%[1] HEC solution	20.4	1.001	4.03×10^3	1.9	17.42	20.30	14.6%	0.5%
4#	0.5% HEC solution	70.2	1.003	1.43×10^4	6.2	59.18	69.01	15.7%	1.7%
5#	0.7% HEC solution	196	1.005	3.09×10^4	12.2	185.22	194.24	5.5%	0.9%
6#	0.9% HEC solution	318	1.007	7.72×10^4	19.8	328.17	327.22	3.2%	2.9%
7#	1.1% HEC solution	543	1.009	9.84×10^4	57.9	557.66	545.72	2.7%	0.5%
8#	1.3% HEC solution	738	1.011	1.27×10^5	75.7	768.26	735.79	4.1%	0.3%
9#	1.5% HEC solution	879	1.013	1.45×10^5	146	918.56	878.91	4.5%	0.01%
10#	1.7% HEC solution	1045	1.015	1.89×10^5	214	1108.76	1083.67	6.1%	3.7%
11#	viscosity standard	466.5	0.839	2.22×10^4	10.1	489.36	463.70	4.9%	0.6%

(1) % means the mass ratio of the hydroxyethyl cellulose (HEC) to water. [2] k_f is calculated by using Eq. (23) and the model described in Section III. k_f/S can be compared with the k_0/S (3.02×10^5 N/m/m^2) to see how the various liquids affect the system stiffness. The viscosity η_a was measured with a commercial viscometer (SV-10, A&D) and the density was measured with a commercial electronic density balance (JA3003J). The storage modulus G' was measured by using a rheometer (Physica MCR 301). η_{m1} and η_{m2} are the viscosities obtained by using the amplitude response and the phase response, respectively.

and

$$D = \frac{S}{m_0}\sqrt{\frac{\eta_f \rho_f}{2}}, \tag{20}$$

Substituting Eqs. (12), (13), and (17)~(20) into Eqs. (13) and (14), we obtain the amplitude and phase responses as

$$A = \frac{h}{[(K_{m_0} - (1 + D\omega^{-1/2})\omega^2)^2 + (\beta_0 + D\omega^{1/2})^2\omega^2]^{1/2}}, \tag{21}$$

$$\phi = \arctan\frac{(\beta_0 + D\omega^{1/2})\omega}{K_{m_0} - (1 + D\omega^{-1/2})\omega^2}. \tag{22}$$

It can be seen from Eqs. (21) and (22) that the amplitude response and phase response are only related to three parameters (β_0, D, K_{m0}). Therefore, by measuring the amplitude and phase responses of the sensor, we can obtain these parameters by means of least-square fitting, and finally the liquid viscosity and the additive stiffness can be calculated from D and K_{m0}, respectively. According to Eq.(20), this approach can only be used to ascertain the product of the fluid density and viscosity ($\rho_f \eta_f$). In order to obtain the liquid viscosity, the liquid density should be known or needs to be measured with other methods.

It is noted that since our modeling approach is based on the assumption that the slice is operated at a perfect shear mode, there may be errors due to the thickness and finite dimension of the slice. The surface tension effect can also introduce errors to the measurement as the device is not fully immersed. A more rigorous model can be developed by following the approach described in Ref. [28], which may help further improve the proposed approach for achieving simultaneous density and viscosity measurements.

IV. RESULTS AND DISCUSSION

As the device was designed to operate at its fundamental mode (at about 44.5 Hz in air) along the X axis, the swept frequency range was from 20 Hz to 65 Hz with 0.3 Hz steps. 11 samples were tested and their property values are listed in TABLE I, covering a dynamic viscosity range from 0.018 mPa·s to 1045 mPa·s. To ensure a good linear relationship between the output voltage of the photodetector and the vibration amplitude, a small excitation voltage was used and the vibration amplitude was limited to be less than 20 μm in the experiment. Both the excitation and response signals were acquired and used to obtain the amplitude and phase responses. The densities of test samples were measured by using a commercial electronic density balance (JA3003J).

Representative measurement results of amplitude and phase responses obtained from 5 different samples are shown in Fig. 7. Through curve fitting of the amplitude and phase response data using Eqs. (21) and (22), respectively, the parameters (β_0, D, K_{m0}) can be obtained. Detailed fitting procedures are provided in supplementary information. For the air case, $D = 0$. Here, we neglect the air damping on both sides of the sensing slice because the product of the air density and viscosity is much smaller than that of the liquid, and this part of the air damping is also significantly smaller than the air damping on other surfaces of the PFHS and the internal damping of the PFHS, which are taken into account as β_0 in Eqs. (21) and (22). We can obtain β_0 and K_{m0_air} by fitting frequency response for the air case. Then we plug β_0 into Eqs. (21) and (22) to perform curve fitting of the frequency responses obtained for other tested liquids and determine the corresponding parameters D and K_{m0_l} for each liquid. Given the liquid density, the viscosity of liquid can be

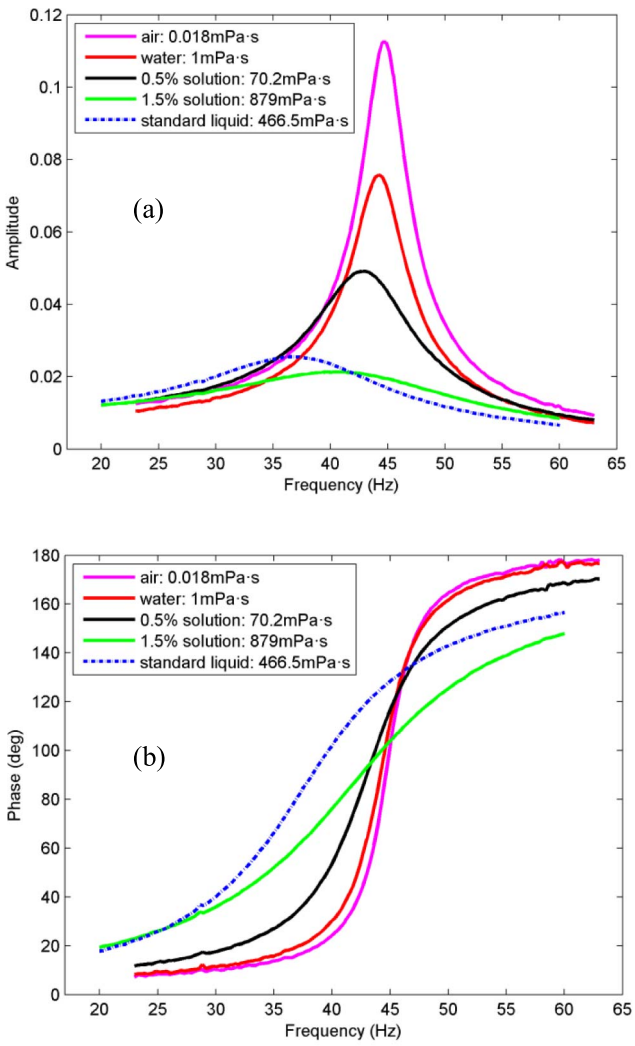

Fig. 7. Representative frequency responses measured with samples of different viscosities: (a) amplitude response and (b) phase response.

calculated from the parameter D, while the additive stiffness can be calculated from K_{m0_l}.

According to Eq. (18), the additive stiffness due to the elasticity of the liquid can be calculated as

$$k_f = m_0(K_{m_0_l} - K_{m_0_air}), \tag{23}$$

where $K_{m_0_air}$ and K_{m0_l} are the K_{m0} values for air and liquid, respectively. The calculated results are listed in TABLE I. It is evident that the stiffness k_f has a large variation among different samples. Compared with the k_0 of 55.2N/m (calculated based on the compliance of 0.0181N/m obtained in Section II-B), the additive stiffness k_f ranges from 1.36% k_0 for the 0.3% HEC solution to 63.4% k_0 for the 1.7% HEC solution.

To investigate how the k_f is related to the elasticity of liquid, experiments were performed to measure the storage and loss moduli [29]–[31] of different HEC solutions listed in TABLE I by using a rheometer (Physica MCR 301). The storage modulus G′ and loss modulus G″ measured at different frequencies are shown in Fig. 8 a and b. The storage modulus G′ is believed to contribute to the liquid elasticity,

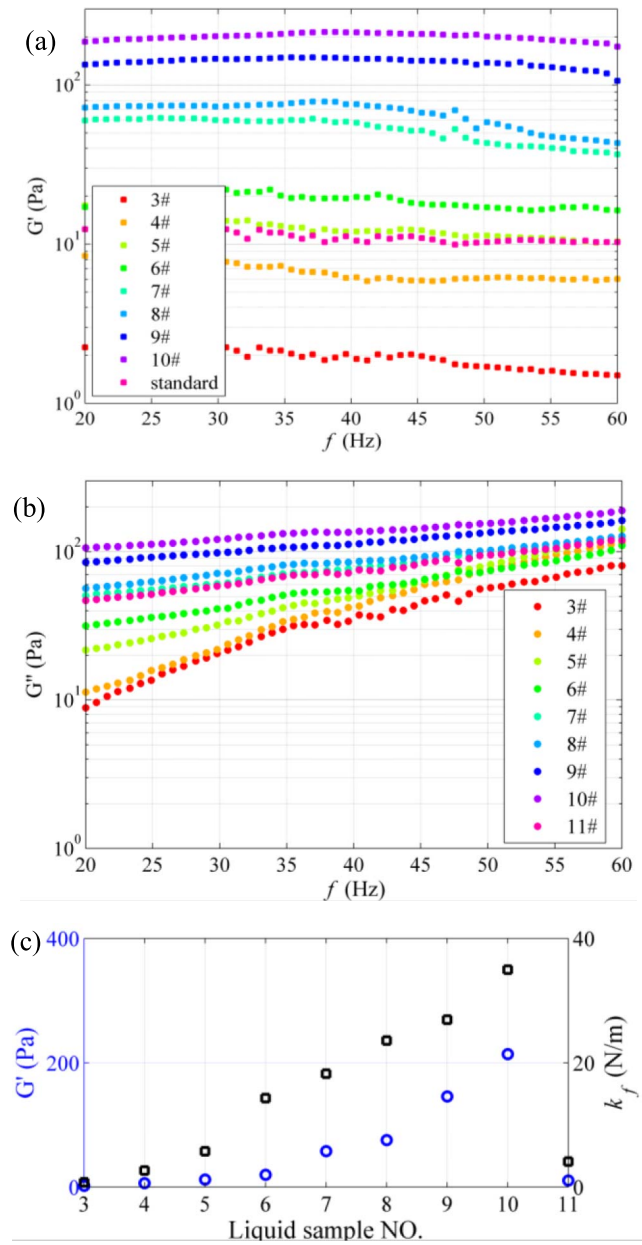

Fig. 8. Measured storage modulus G′ (a) and loss modulus G″ (b) of different liquid samples at different frequencies. (c) Comparison between G′ and k_f at 45 Hz.

while the loss modulus G″ is associated to the liquid viscosity. For all the samples, G′ was found to be almost constant over the measured frequency range of 20 Hz to 60 Hz, while a nearly linear relationship between G″ and f was observed, which is consistent with the results obtained from a previous study [26]. At 45 Hz, G′ and k_f obtained previously are plotted together in Fig. 8 c. The values are listed in TABLE 1. A significant correlation between G′ and the liquid stiffness can be observed: the storage modulus G′ was found to increase with respect to the increase of the additive stiffness. These experimental results indicate that the additive stiffness is mainly caused by the liquid elasticity/storage modulus. Therefore, the additive stiffness is useful for qualitatively characterizing the elastic modulus of liquids.

To determine the viscosity, it should be noted either the amplitude response or the phase response can be used. For the

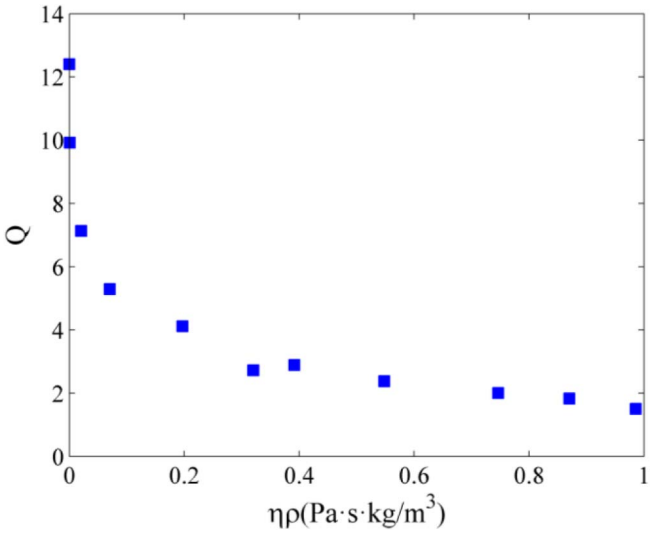

Fig. 9. Quality factor versus product of viscosity and density.

samples listed in TABLE I, the measured viscosities by using both the amplitude and phase responses are compared with those measured with a commercial viscometer (SV-10, A&D). It was found the viscosity determined by using the phase response has better accuracy (with errors less than 3.7%) than that determined by using the amplitude response. Therefore, the phase response was used in the later studies to determine the parameter D and calculate the viscosity.

Next, we compare our approach (i.e., the D parameter method) with the method of using the Q factor to obtain liquid viscosity, which has been reported in the literature [4]. Define the Q factor of the amplitude response curves as

$$Q = \frac{f_r}{\Delta f}, \tag{24}$$

where Δf is the 3 dB bandwidth of the amplitude response curve and f_r is the resonance frequency. The liquid viscosity η can be obtained by performing interpolation on the curve of Q factor as a function of $\eta\rho$. Before measurement, the Q factors of the viscosity sensor in different liquid samples with known viscosity η and density ρ values should be obtained by using the amplitude response curves, which are used to plot the Q-$\eta\rho$ curve. The Q factor versus the product of liquid viscosity and density obtained for samples No. 1∼11 is shown in Fig. 9. The general trend of the curve shows that the Q factor decreases with increasing $\eta\rho$. The next step is to determine the Q factor of the sensor in the liquid with unknown viscosity. Based on this Q factor, the $\eta\rho$ of the liquid can be obtained through performing interpolation based on the pre-determined Q-$\eta\rho$ curve. Finally, if the density is known or can be measured, the viscosity of the liquid can be determined. The results of the proposed method and Q method are listed in TABLE II.

Another common method to determine viscosity is by measuring the resonance frequency [32]. However, this method is only suitable for viscous liquids, but not applicable for viscoelastic liquids, because the resonance frequency is sensitive to the fluid density, viscosity, and elasticity, as shown in Eqs. (12), (13), and (15). Here, we measured the natural

TABLE II

COMPARISION OF RELATIVE ERRORS OF VISCOSITY MEASUREMENT BY USING Q FACTOR AND D PARAMETER AT 20 °C

Test liquids	η_a (mPa·s)	ρ_l (g/cm^3)	Q	D	η_m (mPa·s) by Q	η_m (mPa·s) by D	Relative error (%) by Q	Relative error (%) by D
milk	1.43	1.03	9.8	0.354	1.47	1.429	2.7	0.024
olive oil	102	0.91	5.1	2.986	106	101.5	3.9	1.213
Honey solution	977	1.33	1.6	9.202	957	963.8	2.0	1.346
1% HEC solution	397	1.01	2.6	5.878	404	393.3	1.8	0.93
1.4% HEC solution	826	1.01	1.8	8.479	796	818.4	3.6	0.916
viscosity standard 1	345	0.83	2.7	5.529	360	347.9	4.3	0.828
viscosity standard 2	154	0.84	4.5	3.659	159	152.3	3.2	1.494

η_a represents the viscosity measured by commercial viscometer (SV-10, A&D). η_m represents the viscosity determined from the Q factor or the D parameter. The relative error is determined as $|\eta_m - \eta_a|/\eta_a \times 100\%$. The densities were measured with a commercial electronic density balance (JA3003J).

frequencies and resonance frequencies for the 11 samples listed in TABLE 1, which were obtained from both the amplitude response and phase response curves to confirm the correctness of the results. The results are shown in Fig. 10. f_{nA} and f_{nP} represent the natural frequencies obtained from the amplitude response and the phase response, respectively. f_{dA} and f_{dP} represent the resonance frequencies obtained from the amplitude response and the phase response, respectively. f_{nA}, f_{nP}, f_{dA}, and f_{dP} correspond to samples No. 1∼10. f_{nA2}, f_{nP2}, f_{dA2}, and f_{dP2} correspond to the viscosity standard liquid (sample No. 11). In this case, the results obtained from amplitude and phase responses were found to have similar accuracy.

If the natural frequency is solely determined by the product of the liquid density and viscosity, the obtained natural frequency for the viscosity standard liquid case (sample No. 11) should monotonically follow those obtained for other HEC samples. However, as shown in Fig. 10, the natural frequency for sample No.11 (in green dotted circle) does not follow the trend of other HEC samples (the blue dotted fitting curve).

The reason for sample No. 11 not following the trend of other samples can be explained by the viscoelastic property of liquids. As shown in Fig. 10, for samples No. 3∼10, the natural frequency first decreases, and then saturates, and then increases slightly, as the viscosity increases due to the increase of HEC concentration. This is because the HEC solution is a kind of viscoelastic fluid. Its natural frequency is known as [24]

$$f_n = \frac{\sqrt{\frac{k_0+k_f}{m_0+m_f}}}{2\pi}. \tag{25}$$

At a low concentration/viscosity, the natural frequency is dominated by m_f instead of k_f, and thus the natural frequency (f_{nA} and f_{nP}) decreases as the viscosity increases. At at a high concentration/viscosity, it is dominated by k_f, which

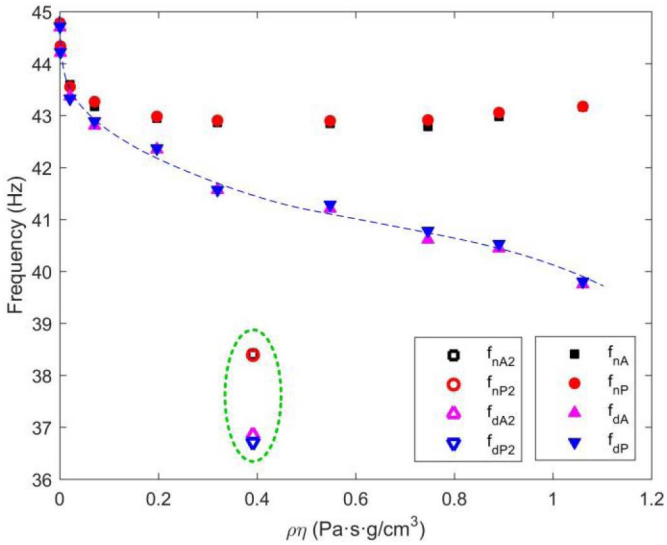

Fig. 10. Resonance frequency and natural frequency versus $\rho\eta$. f_{nA}, f_{nP} represent the natural frequencies obtained from the amplitude response and the phase response, respectively. f_{dA}, f_{dP} represent the resonance frequency obtained from the amplitude response and the phase response, respectively. f_{nA}, f_{nP}, f_{dA}, f_{dP} correspond to sample No. 1∼10 and f_{nA2}, f_{nP2}, f_{dA2}, f_{dP2} correspond to the viscosity standard liquid (sample No. 11).

means the elasticity of the solution cannot be ignored, so the natural frequency (f_{nA} and f_{nP}) increases as the viscosity increases. For sample No.11, its elasticity is negligible, and thus the natural frequency is always dominated by m_f rather than k_f. Therefore, although its viscosity is close to certain HEC samples, the natural frequency for No. 11 is quite different due to its small k_f.

Therefore, compared with the method of measuring the natural frequency or resonance frequency to determine the viscosity, our approach, the D parameter method is applicable for viscoelastic fluids over a large range of viscosities.

V. Conclusions

A viscosity measurement system for viscoelastic fluids based on a miniature 3D printed PFHS and a fiber optic sensor is demonstrated. The PFHS is designed to work as a resonator, which under the excitation of a Lorentz force, will operate at its transverse (X direction) fundamental mode. The structure is highly sensitive to the viscous damping in the X direction and has a strong anti-interference capability as the X-direction compliance is carefully designed to be much larger than those in other directions.

The displacement of the PFHS is measured by using a reflective intensity modulated optic fiber sensor, which utilizes an optical fiber to collect the reflected light intensity from a mirror fixed on the PFHS. The initial distance between the mirror and the optical fiber is chosen to be 760 μm to ensure good linearity and high sensitivity. This all-optical sensor can help effectively eliminate the effect of EMI.

Taking into account the fluid induced mass, damping coefficient, and additive stiffness due to the liquid elasticity, the amplitude and phase responses of the vibrating PFHS are derived and three key parameters (β_0, D, K_{m0}) are identified, which can be directly used to calculate the viscosity and additive stiffness with a given density. In the experiments, by measuring the amplitude and phase responses and performing curve fitting to determine the three key parameters, the viscosity and the additive stiffness are obtained for a number of samples with given mass densities. The storage and loss moduli of the samples are also measured with a commercial system. The experimental results indicate a significant correlation between the additive stiffness and the storage modulus of liquid, which confirms that the additional stiffness is mainly caused by the liquid elasticity/storage modulus. However, further investigation is needed to fully understand the viscoelasticity property of viscoelastic liquid, which is beyond the scope of this work.

Although both the amplitude response and phase response can be used to obtain the viscosity, the proposed method yields more accurate estimates of viscosity when the measured phase response is utilized in lieu of the amplitude response. When utilizing the phase response, the measurement error is found to be less than 3.7% for a wide range of viscosities from 1 mPa·s to 1045 mPa · s.

References

[1] F. Lucklum, E. K. Reichel, and B. Jakoby, "Miniature density–viscosity measurement cell utilizing electrodynamic-acoustic resonator sensors," *Sens. Actuators A, Phys.*, vol. 172, no. 1, pp. 75–81, 2011.

[2] C. A. N. de Castro, F. J. V. Santos, J. M. N. A. Fareleira, and W. A. Wakeham, "Metrology of viscosity: Have we learned enough?" *J. Chem. Eng. Data*, vol. 54, no. 2, pp. 171–178, 2009.

[3] P. Kiełczyński, M. Szalewski, A. Balcerzak, A. J. Rostocki, and D. B. Tefelski, "Application of SH surface acoustic waves for measuring the viscosity of liquids in function of pressure and temperature," *Ultrasonics*, vol. 51, no. 8, pp. 921–924, 2011.

[4] W. Y. Shih, X. Li, H. Gu, W.-H. Shih, and I. A. Aksay, "Simultaneous liquid viscosity and density determination with piezoelectric unimorph cantilevers," *J. Appl. Phys.*, vol. 89, no. 2, pp. 1497–1505, Jan. 2001.

[5] M. Heinisch, E. K. Reichel, I. Dufour, and B. Jakoby, "A resonating rheometer using two polymer membranes for measuring liquid viscosity and mass density," *Sens. Actuators A, Phys.*, vol. 172, no. 1, pp. 82–87, 2011.

[6] A. Abdallah, M. Heinisch, and B. Jakoby, "Viscosity measurement cell utilizing electrodynamic-acoustic resonator sensors: Design considerations and issues," *Procedia Eng.*, vol. 47, pp. 160—164, Sep. 2012.

[7] E. K. Reichel, M. Heinisch, and B. Jakoby, "Fluid property sensors," *Resonant MEMS, Fundamentals, Implementation and Application* (Advanced Micro and Nanosystems), vol. 11, O. Brand, I. Dufour, S. M. Heinrich, and F. Josse, Eds. New York, NY, USA: Wiley, 2015, pp. 427–450, ch. 17.

[8] M. K. Ghatkesara, E. Rakhmatullina, H.-P. Lang, C. Gerber, M. Hegner, and T. Braun, "Multi-parameter microcantilever sensor for comprehensive characterization of Newtonian fluids," *Sens. Actuators B, Chem.*, vol. 135, no. 1, pp. 133–138, Dec. 2008.

[9] C. Riesch *et al.*, "A suspended plate viscosity sensor featuring in-plane vibration and piezoresistive readout," *J. Micromech. Microeng.*, vol. 19, no. 7, p. 075010, 2009.

[10] M. Heinisch, E. K. Reichel, I. Dufour, and B. Jakoby, "Tunable resonators in the low kHz range for viscosity sensing," *Sens. Actuators A, Phys.*, vol. 186, pp. 111–117, Oct. 2012.

[11] M. Heinisch, T. Voglhuber-Brunnmaier, A. Niedermayer, B. Jakoby, and E. K. Reichel, "Double membrane sensors for liquid viscosity and mass density facilitating measurements in a large frequency range," in *Proc. IEEE Sensors Conf.*, vol. 143. Nov. 2010, pp. 1750–1753.

[12] C. Riesch and B. Jakoby, "Novel readout electronics for thickness shear-mode liquid sensors compensating for spurious conductivity and capacitances," *IEEE Sensors J.*, vol. 7, no. 3, pp. 464–469, Mar. 2007.

[13] V. Raimbault, D. Rebière, and C. Dejous, "A microfluidic surface acoustic wave sensor platform: Application to high viscosity measurements," *Mater. Sci. Eng.*, vol. 28, nos. 5–6, pp. 759–764, 2008.

[14] R. Beigelbeck, H. Antlinger, S. Ćerimović, S. Clara, F. Keplinger, and B. Jakoby, "Resonant pressure wave setup for simultaneous sensing of longitudinal viscosity and sound velocity of liquids," *Meas. Sci. Technol.*, vol. 24, no. 1, p. 125101, Oct. 2013.
[15] A. Balcerzak, M. Aleksiejuk, G. Zhavnerko, and V. Agabekov, "Sensing properties of two-component Langmuir–Blodgett layer and its porous derivative in SAW sensor for vapors of methanol and ethanol," *Thin Solid Films*, vol. 518, no. 12, pp. 3402–3406, 2010.
[16] M. Heinisch, T. Voglhuber-Brunnmaier, E. K. Reichel, I. Dufour, and B. Jakoby, "Application of resonant steel tuning forks with circular and rectangular cross sections for precise mass density and viscosity measurements," *Sens. Actuators A, Phys.*, vol. 226, pp. 163–174, May 2015.
[17] G. W. Northey, M. L. Oliver, and D. M. Rittenhouse, "Calibration of a Hall effect displacement measurement system for complex motion analysis using a neural network," *J. Biomech.*, vol. 39, no. 10, pp. 1943–1947, 2006.
[18] S. Xia and S. Nihtianov, "Power-efficient high-speed and high-resolution capacitive-sensor interface for subnanometer displacement measurements," *IEEE Trans. Instrum. Meas.*, vol. 61, no. 5, pp. 1315–1322, May 2012.
[19] H. Wang, B. Ju, W. Li, and Z. Feng, "Ultrastable eddy current displacement sensor working in harsh temperature environments with comprehensive self-temperature compensation," *Sens. Actuators A, Phys.*, vol. 211, pp. 98–104, May 2014.
[20] S.-J. Chen and S.-S. Pan, "A force measurement system based on an electrostatic sensing and actuating technique for calibrating force in a micronewton range with a resolution of nanonewton scale," *Meas. Sci. Technol.*, vol. 22, no. 4, p. 045104, 2011.
[21] W. Xu and T. King, "Flexure hinges for piezoactuator displacement amplifiers: Flexibility, accuracy, and stress considerations," *Precis. Eng.*, vol. 19, no. 1, pp. 4–10, 1996.
[22] S. T. Smith, V. G. Badami, J. S. Dale, and Y. Xu, "Elliptical flexure hinges," *Review of Scientific Instruments*, vol. 68, no. 3, p. 1474, 1997.
[23] G. Chen, X. Shao, and X. Huang, "A new generalized model for elliptical arc flexure hinges," *Rev. Sci. Instrum.*, vol. 79, no. 9, p. 095103, 2008.
[24] B. Balachandran and E. B. Magrab, *Vibrations*, 2nd ed. Boston, MA, USA: Cengage Learning, 2009.
[25] C. Castelain, J. L. Doublier, and J. Lefebvre, "A study of the viscosity of cellulose derivatives in aqueous solutions," *Carbohydrate Polym.*, vol. 7, no. 1, pp. 1–6, 1987.
[26] D. Hadjistamov, "Oscillatory measurements of silicone oils—Loss and storage modulus master curves," *Rheol. Acta*, vol. 35, no. 4, pp. 364–368, 1996.
[27] E. K. Reichel, C. Riesch, F. Keplinger, C. E. A. Kirschhock, and B. Jakoby, "Analysis and experimental verification of a metallic suspended plate resonator for viscosity sensing," *Sens. Actuators A, Phys.*, vol. 162, no. 2, pp. 418–424, 2010.
[28] M. Heinisch, T. Voglhuber-Brunnmaier, E. K. Reichel, I. Dufour, and B. Jakoby, "Reduced order models for resonant viscosity and mass density sensors," *Sens. Actuators A, Phys.*, vol. 220, pp. 76–84, Dec. 2014.
[29] N. E. Kiratzis and P. F. Luckham, "The rheology of aqueous alumina suspensions in the presence of hydroxyethyl cellulose as binder," *J. Eur. Ceram. Soc.*, vol. 19, pp. 2605–2612, 1999.
[30] P. Kiełczyński, W. Pajewski, M. Szalewski, and A. Balcerzak, "Measurement of the shear storage modulus and viscosity of liquids using the Bleustein–Gulyaev wave," *Rev. Sci. Instrum.*, vol. 75, no. 7, pp. 2362–2367, 2004.
[31] R. Pal, "Complex shear modulus of concentrated suspensions of solid spherical particles," *J. Colloid Interface Sci.*, vol. 245, no. 1, pp. 171–177, 2002.
[32] A. O. Niedermayer, T. Voglhuber-Brunnmaier, J. Sell, and B. Jakoby, "Methods for the robust measurement of the resonant frequency and quality factor of significantly damped resonating devices," *Meas. Sci. Technol.*, vol. 23, no. 8, p. 085107, 2012.

Jinyu Ma received the B.S. and M.S. degrees from the Shandong University of Science and Technology, China, in 2010 and 2012, respectively. From 2014 to 2015, she was a Visiting Student with the University of Maryland, USA. She is currently pursuing the Ph.D. degree with Tianjin University, China. Her research topic is fiber optic sensing and viscosity measurement.

Xinjing Huang received the B.S. degree from Tianjin University, China, in 2010, where he is currently pursuing the Ph.D. degree. His research interests involve computational sensing, measurement and control technology, and smart instrumentation.

Hyungdae Bae received the B.S. and M.S. degrees from Yonsei University, Seoul, South Korea, in 2004 and 2006, respectively, and the Ph.D. degree from the University of Maryland in 2013, all in mechanical engineering. He is a Research Assistant with the Mechanical Engineering Department, University of Maryland. His current research interests include miniature fiber optic pressure/temperature sensor, temperature compensation of fiber optic sensors, and micro/nanofabrication of optical element based on polymer processing.

Yelong Zheng received the M.S. and Ph.D. degrees from Tianjin University, China, in 2012 and 2015, respectively. Since 2015, he has been a Post-Doctor with Tsinghua University. His current research interests include microforce measurement and vivo sensitive measuring forces and tribology.

Cong Liu received the bachelor's degree from the Yanshan University of China in 2012. She is currently pursuing the master's degree with Tianjin University, China. Her research work includes circuit design in flexible hinge system and experimental measurement of liquid viscosity.

Meirong Zhao received the M.S. and Ph.D. degrees from Tianjin University (TJU), China, in 1993 and 1996, respectively. She is a Professor with the State Key Laboratory of Precision Measuring Technology and Instruments, TJU. Her interests include photoelectric measurement and control technology, visual inspection, and micro–nano measurement.

Miao Yu received the Ph.D. degree from the University of Maryland (UMD) in 2002. She is currently an Associate Professor with the Department of Mechanical Engineering, UMD, with an expanded range of research interests encompassing bio-inspired systems, sensors and actuators, light and matter interactions, plasmonics and metamaterials, microsystems and nanosystems, and smart materials and structures. Her awards and honors include receipt of the 2006 Ralph E. Powe Junior Faculty Enhancement Award (2006), the NSF CAREER Award (2007), and the AFOSR Young Investigator Award (2008).